

Robust Simultaneous Multislice MRI Reconstruction Using Deep Generative Priors

Shoujin Huang, Guanxiong Luo, Yuwan Wang, Kexin Yang, Lingyan Zhang, Jingzhe Liu, Hua Guo, Min Wang, and Mengye Lyu

Abstract—Simultaneous multislice (SMS) imaging is a powerful technique for accelerating magnetic resonance imaging (MRI) acquisitions. However, SMS reconstruction remains challenging due to the complex signal interactions between and within the excited slices. This study presents a robust SMS MRI reconstruction method using deep generative priors. Starting from Gaussian noise, we leverage denoising diffusion probabilistic models (DDPM) to gradually recover the individual slices through reverse diffusion iterations while imposing data consistency from the measured k-space under readout concatenation framework. The posterior sampling procedure is designed such that the DDPM training can be performed on single-slice images without special adjustments for SMS tasks. Additionally, our method integrates a low-frequency enhancement (LFE) module to address a practical issue that SMS-accelerated fast spin echo (FSE) and echo-planar imaging (EPI) sequences cannot easily embed autocalibration signals. Extensive experiments demonstrate that our approach consistently outperforms existing methods and generalizes well to unseen datasets. The code is available at <https://github.com/Solor-pikachu/ROGER> after the review process.

Index Terms—Simultaneous multislice, MRI reconstruction, Diffusion model

I. INTRODUCTION

Accelerating magnetic resonance imaging (MRI) is important for capturing subtle spatial/temporal information, im-

This work was supported in part by the National Natural Science Foundation of China under Grant 62101348 and Shenzhen Higher Education Stable Support Program (Shenzhen Science and Technology Program) under Grant 20220716111838002. (Corresponding authors: Lingyan Zhang; Mengye Lyu.)

Shoujin Huang, Wang Yuwan, Kexin Yang, and Mengye Lyu are with the College of Health Science and Environmental Engineering, Shenzhen Technology University, Shenzhen, China (email: lv-mengye@sztu.edu.cn).

Guanxiong Luo is with Institute for Diagnostic and Interventional Radiology, University Medical Center Göttingen, Göttingen, Germany.

Lingyan Zhang is with the Lab of Molecular Imaging and Medical Intelligence, Department of Radiology, Longgang Central Hospital of Shenzhen, Shenzhen, China, also with the Shenzhen Clinical Medical College, Guangzhou University of Chinese Medicine, Shenzhen, China, and also with the Longgang Central Hospital of Shantou University Medical College, Shenzhen, China (email:18819818005@163.com).

Jingzhe Liu is with the Department of Radiology, the First Hospital of Tsinghua University, Beijing, China.

Hua Guo is with the Center for Biomedical Imaging Research, Department of Biomedical Engineering, School of Medicine, Tsinghua University, Beijing, China.

Min Wang is with Key Laboratory for Biomedical Engineering of Ministry of Education, College of Biomedical Engineering and Instrument Science, Zhejiang University, Hangzhou, China.

proving patient throughput, and minimizing motion artifacts. Simultaneous multislice (SMS) imaging [1]–[4] addresses this by using multiband (MB) radio-frequency pulses to acquire multiple slices simultaneously, effectively reducing scan time and/or improving slice coverage. Unlike in-plane acceleration, which suffers from intrinsic signal-to-noise ratio (SNR) loss due to k-space undersampling, SMS acquisitions benefit from improved SNR efficiency due to Fourier averaging [4].

Despite its advantages, SMS MRI presents considerable reconstruction challenges. The simultaneous acquisition of multiple slices results in inter-slice signal interactions and potential artifacts. Traditional SMS reconstruction methods [1], [3], [5]–[7] are adapted from classical parallel imaging techniques, often suffering from noise amplification and residual aliasing artifacts. Improved iterative approaches [8]–[12], introduce additional regularization to stabilize the reconstruction but still struggle with ill-conditioning at high acceleration settings.

Recent advancements in deep learning have shown promise for improving MRI reconstruction quality [13]. Supervised learning methods [14]–[16], have been successfully demonstrated on in-plane accelerated MRI, leveraging large datasets to learn the reconstruction mappings. These models may also be adapted to SMS reconstruction by training on SMS-accelerated and fully sampled k-space pairs [17] or in self-supervised manners [18]. However, supervised deep learning methods may not generalize well to unseen data, such as those with different acquisition parameters, aliasing patterns, and coil sensitivity distributions.

Recently, the use of generative models has emerged as a potentially more robust approach for MRI reconstruction [19]–[26]. Generative models can learn data distributions as priors in solving the inverse problem of MR reconstruction. This flexibility allows generative models to adapt to a variety of MRI reconstruction tasks. However, the application of generative models to SMS reconstruction has not been studied to the best of our knowledge, and this is not straightforward for the following reasons.

Firstly, the forward model of SMS imaging is not conventional k-space subsampling. This process includes encoding multiple 2D slices by different coil sensitivity maps, phase cycling for Controlled Aliasing in Parallel Imaging Results in Higher Acceleration (CAIPI) shifts [1], and the summation of signals into a single 2D matrix. This complexity, combined with the variations in MB factors (number of simultaneously

acquired slices), CAIPI shift patterns, and additional in-plane acceleration factors, results in a wide range of aliasing patterns.

Secondly, SMS acceleration is desirable across diverse MRI applications, including anatomical imaging and functional/diffusion-weighted imaging [27], [28]. These applications may have very different imaging parameters, tissue contrast and resolution requirements. For instance, T2-FSE anatomical imaging typically uses large matrix sizes over 300, while EPI often uses smaller matrix sizes around 100. Ensuring high-quality reconstructions across these scenarios necessitates highly robust reconstruction methods.

Thirdly, it is difficult to acquire slice-wise autocalibration signals (ACS), i.e., fully sampled central k-space, within the SMS-accelerated scans. This is particularly problematic in Cartesian fast-spin-echo (FSE) [29] and echo-planar imaging (EPI) [3], [7], [18] sequences, which acquire echo trains while T2/T2* decay occurs. In FSE, integrating ACS complicates phase encoding and requires careful optimization to address signal discontinuities. In EPI, uniform k-space sampling is preferred to reduce geometric distortions [30]. Therefore, a fast single-band scan is typically used to provide coil sensitivity maps or GRAPPA kernels for SMS reconstruction, but these calibration scans usually have different tissue contrasts and image phases, such that they cannot be directly merged into the SMS data to provide low-frequency information, rendering reconstruction challenging.

To address these challenges, we propose a novel SMS MRI reconstruction method based on denoising diffusion probabilistic models (DDPM) and validate it through extensive experiments in this study. The contributions are summarized as follows:

- We present a new reconstruction method that employs deep generative priors to disentangle mixed slices in SMS MRI. We name this method ROGER (SMS reconstruction using ReadOut concatenation and deep GENEraTive priors).
- We propose a Low-Frequency Enhanced Module (LFE) that stabilizes the reverse diffusion process, particularly benefiting widely used SMS-accelerated FSE and EPI sequences that cannot easily integrate ACS.
- Compared with existing methods, our method demonstrates substantially improved image SNR, fewer artifacts and excellent generalization ability across five datasets under various settings.

II. BACKGROUND

A. Related Work and Problem Formulation

SMS MRI reconstruction can be approached using several different frameworks [2], [3], [5], [31]–[33] for handling the complexities of SMS encoding and signal separation.

Classical slice-SENSE method [32] utilizes known coil sensitivity profiles to separate signals from simultaneously acquired slices in pure image domain. GRAPPA-based methods [34] offer another approach to SMS reconstruction based on k-space interpolation. While SENSE-GRAPPA [5] extends the field of view (FOV) along phase encoding direction and

applies traditional GRAPPA methods to solve for aliased signals, slice-GRAPPA [3] reconstructs the data directly into separated slices without needing to create an extended FOV. An improved implementation of slice-GRAPPA is split slice-GRAPPA (SPSG) [7], which trains kernels not only to reconstruct the target slice but also suppress erroneous mappings to other slices. This approach mitigates slice leakage issue and improves temporal signal-to-noise ratio (tSNR).

SMS reconstruction can also be reformulated using the readout concatenation framework [2], [9], [35]–[37], which transforms SMS encoding as a one-dimensional in-plane acceleration along the readout direction. In this approach, the slices to be reconstructed are viewed as spatially concatenated, forming a single 2D image with the FOV extended MB times along the readout direction. Consequently, SMS acceleration can be characterized as a uniform k-space subsampling in this extended readout direction, with optional in-plane undersampling incorporated in the phase encoding dimension. Thus, the forward model for ROC based SMS reconstruction is given by:

$$\mathbf{y} = \mathcal{A}\bar{\mathbf{x}}^{ms} + \eta \quad (1)$$

, where $\bar{\mathbf{x}}^{ms} = \{\bar{\mathbf{x}}^1, \bar{\mathbf{x}}^2, \bar{\mathbf{x}}^3, \dots, \bar{\mathbf{x}}^{MB}\}$ are the slice images to be reconstructed, MB is the number of simultaneously acquired slices, η is complex Gaussian noise, \mathcal{R} represents the combined data reorder operations of \mathcal{ROC} (readout concatenation) and \mathcal{CS} (CAIPI shift), and \mathcal{A} is SENSE encoding operator. \mathcal{A} can be further breakdown to $\mathcal{P} \cdot \mathcal{F} \cdot \mathcal{S}$ where \mathcal{F} is two-dimensional Fourier transform, \mathcal{S} coil sensitivity maps, and \mathcal{P} k-space subsampling. We adopt this ROC framework for applying SMS data consistency terms in this study.

B. Denoising Diffusion Probabilistic Models

Diffusion models are probabilistic generative models that express image generation as a temporal Markov process. DDPM defines a T -step forward and reverse diffusion process [38]. The forward process adds random Gaussian noise to image, while the reverse process constructs desired data samples from the Gaussian noise.

1) *Forward Diffusion*: The forward process yields the present state \mathbf{x}_t from the previous state \mathbf{x}_{t-1} . At step t , the relationship between t and $t-1$, along with the conditional distribution $q(\mathbf{x}_t | \mathbf{x}_{t-1})$, is specified as follows:

$$q(\mathbf{x}_t | \mathbf{x}_{t-1}) = \mathcal{CN}(\mathbf{x}_t; \sqrt{1 - \beta_t}\mathbf{x}_{t-1}, \beta_t \mathbf{I}) \quad (2)$$

$$\mathbf{x}_t = \sqrt{1 - \beta_t}\mathbf{x}_{t-1} + \sqrt{\beta_t}\mathbf{z}, \mathbf{z} \sim \mathcal{CN}(0, \mathbf{I}), \quad (3)$$

where β_t follows a pre-defined schedule $\{\beta_0, \beta_1, \dots, \beta_T\}$ which is an increasing sequence of t . \mathbf{x}_t converges to isotropic Gaussian noise after a large number of forward steps. Following re-parameterization method [39], the two equations become:

$$q(\mathbf{x}_t | \mathbf{x}_0) = \mathcal{CN}(\mathbf{x}_t; \sqrt{\bar{a}_t}\mathbf{x}_0, (1 - \bar{a}_t)\mathbf{I}) \quad (4)$$

$$\mathbf{x}_t = \sqrt{\bar{a}_t}\mathbf{x}_0 + \sqrt{1 - \bar{a}_t}\mathbf{z}, \mathbf{z} \sim \mathcal{CN}(0, \mathbf{I}), \quad (5)$$

with $\bar{a}_t := \prod_{s=1}^t a_s$, $a_t := 1 - \beta_t$. Intuitively for every training step, DDPM randomly picks a clean image \mathbf{x}_0 from the high-quality dataset and samples a noise $\mathbf{z} \sim \mathcal{CN}(0, \mathbf{I})$, then picks

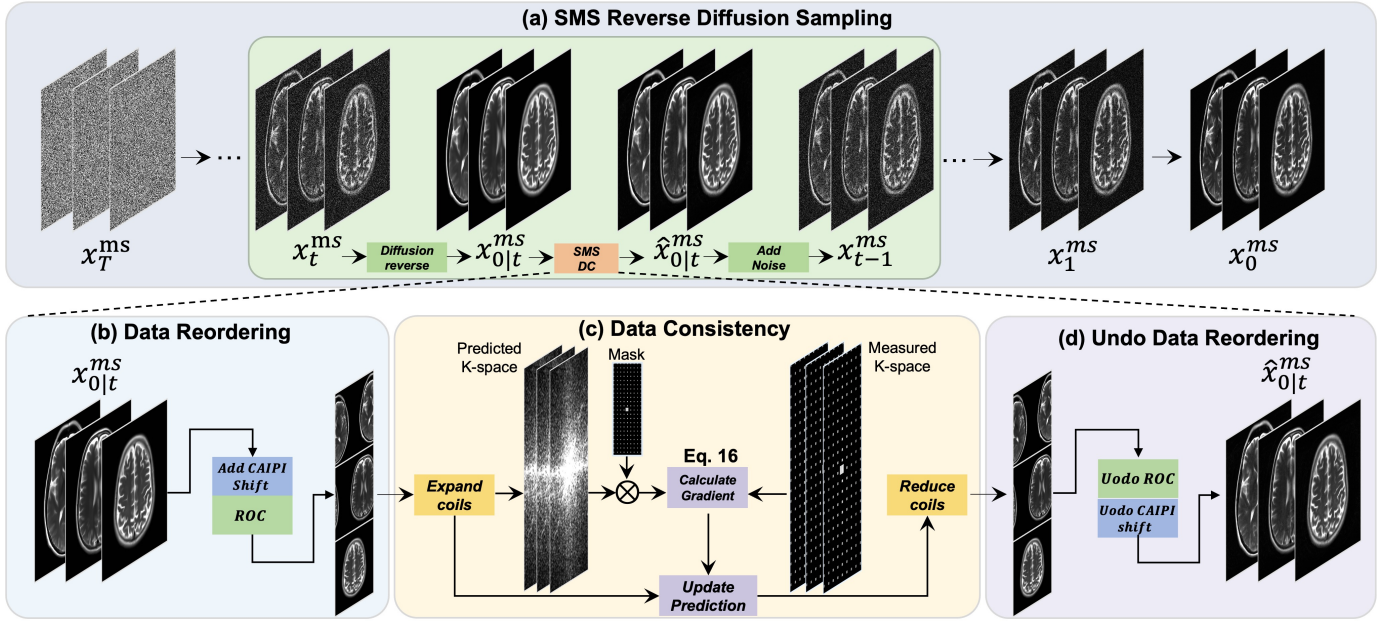


Fig. 1. Schematic illustration of the proposed ROGER method. (a) The overall reconstruction procedure using reverse diffusion sampling: at each reverse diffusion sampling timestep t , the image estimate $\mathbf{x}_{0|t}^{ms}$ is refined from \mathbf{x}_t^{ms} using pre-trained denoising model via Eq. 11, followed by an adjustment with the SMS data consistency (DC) term from Eq. 12. Noise is then added to $\hat{\mathbf{x}}_{0|t}^{ms}$ to compute \mathbf{x}_{t-1}^{ms} for the next sampling step as per Eq. 13. The SMS DC process includes (b) Data Reordering \mathcal{R} , which applies CAIPI shift and readout concatenation (ROC) to $\mathbf{x}_{0|t}^{ms}$, (c) Data Consistency, which updates $\mathcal{R}\mathbf{x}_{0|t}^{ms}$ using the gradient of the DC term, and (d) Undo Data Reordering \mathcal{R}^H , which reverses the reordering process to derive $\hat{\mathbf{x}}_{0|t}^{ms}$, facilitating continuation of the reverse diffusion sampling.

a random time-step t and updates the network parameters θ in ϵ_θ^t to minimize the following expectation:

$$\min \mathbb{E}_{\mathbf{x}_t \sim q(\mathbf{x}_t | \mathbf{x}_0), \mathbf{x}_0 \sim p_{data}(\mathbf{x}_0), \mathbf{z} \sim \mathcal{CN}(0, \mathbf{I})} \|\epsilon_\theta^t(\mathbf{x}_t - \mathbf{z})\|_2^2 \quad (6)$$

Usually, DDPM uses a neural network ϵ_θ^t is to predict the noise \mathbf{z} for each time-step t .

2) Reverse diffusion: The reverse process aims at yielding the previous state \mathbf{x}_{t-1} from \mathbf{x}_t using the posterior distribution $p(\mathbf{x}_{t-1} | \mathbf{x}_t, \mathbf{x}_0)$, which can be derived from the Bayes theorem from Eqs. 4 and 5:

$$\begin{aligned} p(\mathbf{x}_{t-1} | \mathbf{x}_t, \mathbf{x}_0) &= q(\mathbf{x}_t | \mathbf{x}_{t-1}) \frac{q(\mathbf{x}_{t-1} | \mathbf{x}_0)}{q(\mathbf{x}_t | \mathbf{x}_0)} \\ &= \mathcal{CN}(\mathbf{x}_{t-1}; \mu_t(\mathbf{x}_t, \mathbf{x}_0), \sigma_t^2 \mathbf{I}) \end{aligned} \quad (7)$$

with the closed forms of mean $\mu_t(\mathbf{x}_t, \mathbf{x}_0) = \frac{1}{\sqrt{a_t}}(\mathbf{x}_t - \frac{1-a_t}{\sqrt{1-a_t}}\epsilon_\theta^t(\mathbf{x}_t))$, and variance $\sigma_t^2 = \frac{1-\bar{a}_{t-1}}{1-\bar{a}_t}\beta_t$. Hence, we have

$$\mathbf{x}_{t-1} = \frac{1}{\sqrt{a_t}}(\mathbf{x}_t - \frac{1-a_t}{\sqrt{1-a_t}}\epsilon_\theta^t(\mathbf{x}_t)) + \frac{1-\bar{a}_{t-1}}{1-\bar{a}_t}\beta_t \mathbf{z} \quad (8)$$

We adopt denoising diffusion implicit model (DDIM) [40] as the reverse sampling method, which is a variant of standard DDPM and faster than it. In DDIM, the reverse diffusion is :

$$\mathbf{x}_{0|t} = \frac{1}{\sqrt{a_t}}(\mathbf{x}_t - \sqrt{1-\bar{a}_t}\epsilon_\theta^t(\mathbf{x}_t)) \quad (9)$$

$$\mathbf{x}_{t-1} = \sqrt{\bar{a}_{t-1}}\mathbf{x}_{0|t} + \sqrt{1-\bar{a}_{t-1}}\mathbf{z} \quad (10)$$

where $\mathbf{x}_{0|t}$ as the denoised estimate \mathbf{x}_t at time-step t . By iteratively sampling \mathbf{x}_{t-1} from $p(\mathbf{x}_{t-1} | \mathbf{x}_t, \mathbf{x}_0)$, DDPM can yield clean images $\mathbf{x}_0 \sim q(\mathbf{x})$ from random Gaussian noises

$\mathbf{x}_T \sim \mathcal{CN}(0, \mathbf{I})$, where $q(\mathbf{x})$ is the approximation of the distribution of training data.

III. METHODOLOGY

A. SMS Reverse Diffusion Sampling

Alike many diffusion model-based techniques, reconstruction is one of the samples from the posterior distribution which is formulated with two components: 1) the likelihood term to describe the data consistency; 2) the diffusion prior trained on image dataset.

As illustrated in Fig. 1, our proposed SMS reconstruction ROGER employs DDPM to provide slice-wise learned probability distributions [22], [41], and the data consistency terms are applied through ROC framework.

Given multi-coil measurements \mathbf{y} which are acquired SMS data across all coils, our goal is to find proper $\bar{\mathbf{x}}^{ms}$ that contains the slices $\{\bar{\mathbf{x}}^1, \bar{\mathbf{x}}^2, \bar{\mathbf{x}}^3, \dots, \bar{\mathbf{x}}^{MB}\}$ satisfying Eq. 1.

From Eq. 9, we initialize the \mathbf{x}_t^{ms} from random noise $\mathbf{z} \sim \mathcal{CN}(0, \mathbf{I})$, and the reverse diffusion process is

$$\mathbf{x}_{0|t}^{ms} = \frac{1}{\sqrt{a_t}}(\mathbf{x}_t^{ms} - \sqrt{1-\bar{a}_t}\epsilon_\theta^t(\mathbf{x}_t^{ms})) \quad (11)$$

For MRI reconstruction and more general image restoration tasks, it is required to equip the iterations with data consistency (fidelity) guidance [19]–[25], [42]–[46]. This guidance is typically based on the gradient of a data consistency term. Hence, to finally yield \mathbf{x}_0^{ms} satisfying $\mathcal{A}\mathcal{R}\mathbf{x}_0^{ms} = \mathbf{y}$, we enforce that $\mathbf{x}_{0|t}^{ms}$ satisfies the data consistency constraint $(\mathcal{A}\mathcal{R})^H \mathcal{A}\mathcal{R}\mathbf{x}_{0|t}^{ms} = (\mathcal{A}\mathcal{R})^H \mathbf{y}$, and thus we have

$$\hat{\mathbf{x}}_{0|t}^{ms} = \mathbf{x}_{0|t}^{ms} - \lambda(\mathcal{A}\mathcal{R})^H(\mathcal{A}\mathcal{R}\mathbf{x}_{0|t}^{ms} - \mathbf{y}) \quad (12)$$

where $(\mathcal{AR})^H$ denotes the adjoint-inverse of \mathcal{AR} and λ is the guidance scaling factor. This hyperparameter λ is fixed to be 2 in this study. Then we based on Eq. 10 yield the previous \mathbf{x}_{t-1}^{ms} by sampling from $p(\mathbf{x}_{t-1}^{ms} | \mathbf{x}_t^{ms}, \hat{\mathbf{x}}_{0|t}^{ms})$.

$$\mathbf{x}_{t-1}^{ms} = \sqrt{\bar{a}_{t-1}} \hat{\mathbf{x}}_{0|t}^{ms} + \sqrt{1 - \bar{a}_{t-1}} \mathbf{z}, \mathbf{z} \sim \mathcal{CN}(0, \mathbf{I}). \quad (13)$$

By applying Eqs. 11, 12 and 13 sequentially and iteratively, we can yield samples from $q(\mathbf{x})$ constrained by $\mathcal{AR}(\mathbf{x}_0) = \mathbf{y}$.

B. Low-Frequency Enhanced Module

In practice, SMS-accelerated FSE and EPI sequences cannot easily embed autocalibration signals (ACS). The absence of low-frequency renders reconstruction challenging as the information for object shape and tissue contrasts is not available. To address this issue, we propose a simple yet effective low-frequency enhancement (LFE) method that uses GRAPPA to interpolate in the central k-space of the ROC data. Specifically, we first estimate the GRAPPA kernels from a calibration scan.

$$kernel_\theta \xleftarrow{\text{GRAPPA}} \mathcal{R}(\text{calibrations}) \quad (14)$$

The estimated $kernel_\theta$ are then utilized to predict the missing k-space points in the low-frequency region:

$$\mathbf{y}' = \text{LFE}_s(kernel_\theta, \mathbf{y}) \quad (15)$$

where s is the LFE size, i.e., size of estimated low-frequency area. This hyperparameter is fixed to be 8 in this study. The mask in \mathcal{A} will be updated to preserve both the LFE estimated and original data.

In summary, our reconstruction algorithm can be described with the pseudo code below.

Algorithm 1 SMS Reverse Diffusion Sampling

Require: $kernel_\theta$, calibrations, measurement \mathbf{y} , forward model \mathcal{A} , reorder \mathcal{R} , LFE size s , guidance scaling factor λ .

```

1:  $kernel_\theta \xleftarrow{\text{GRAPPA}} \mathcal{R}(\text{calibrations})$ 
2:  $\mathbf{y}' = \text{LFE}_s(kernel_\theta, \mathbf{y})$ 
3:  $\mathbf{x}_T^{ms} \sim \mathcal{CN}(0, \mathbf{I})$ 
4: for  $t = T$  to 0 do
5:    $\mathbf{x}_{0|t}^{ms} = \frac{1}{\sqrt{a_t}}(\mathbf{x}_t^{ms} - \sqrt{1 - \bar{a}_t} \epsilon_\theta^t(\mathbf{x}_t^{ms}))$ 
6:    $\hat{\mathbf{x}}_{0|t}^{ms} = \mathbf{x}_{0|t}^{ms} - \lambda(\mathcal{AR})^H(\mathcal{AR}\mathbf{x}_{0|t}^{ms} - \mathbf{y}')$ 
7:    $\mathbf{x}_{t-1}^{ms} = \sqrt{\bar{a}_{t-1}} \hat{\mathbf{x}}_{0|t}^{ms} + \sqrt{1 - \bar{a}_{t-1}} \mathbf{z}, \mathbf{z} \sim \mathcal{CN}(0, \mathbf{I})$ 
8: end for
9: return  $\mathbf{x}_0^{ms}$ 

```

IV. EXPERIMENTS

A. Datasets

First, three raw k-space datasets were used with retrospective SMS acceleration to evaluate our method:

- 1) The public fastMRI brain dataset [47]. In brief, this dataset includes brain anatomical imaging data acquired on 1.5T and 3T magnets. The official training set was used to train our model (see "Method Comparison and Implementation Details" for details). In the training

set, the majority were T2-weighted scans (2678 volumes), with the rest being T1-weighted (1447 volumes) and fluid attenuated inversion recovery (FLAIR) scans (344 volumes). We randomly selected 16 scans of T2-weighted contrast from the official validation set for method evaluation. Note that for data de-identification, this dataset does not contain any slices more than 5mm below the orbital rim [47].

- 2) An in-house clinical dataset (Longgang). It included T1-weighted and T2-FLAIR images from 8 subjects with white matter lesions, acquired using a 3T Siemens scanner equipped with a 20-channel head coil. The common scan parameters were FOV = 220 mm and slice thickness/gap = 5/1.5 mm. For T1-weighted scans, TR/TE = 250/2.49 ms, flip angle (FA) = 70°, and matrix size = 320×288. For FLAIR, TR/TE/TI = 8000/84/2370 ms, refocusing FA = 150°, and matrix size = 320×224.
- 3) An in-house T2-FSE dataset (Huaxin) from 4 healthy volunteers using a 3T GE scanner equipped with a 21-channel head coil. This dataset has whole brain coverage including the cerebellum and brainstem. The scan parameters were TR/TE = 4784/100 ms, refocusing FA = 111°, matrix size = 256×256, FOV = 220 mm, slice thickness/gap = 3/0.3 mm, 48 slices.

For retrospective acceleration, we experimented with MB factors of 3 and 4, and in-plane acceleration R factors of 2 and 3, resulting in four acceleration combinations: MB3R2, MB3R3, MB4R2, and MB4R3. This notation, MBxRy, will be used in the following sections to denote the specific acceleration settings.

Additionally, two prospectively SMS-accelerated datasets were used to further validate our methods:

- 1) Prospectively SMS-accelerated T2-FSE data from one healthy subject at MB3R3 and MB4R2 using a 3T Siemens scanner equipped with a 64-channel head coil. The scan parameters were TR/TE = 6000/100 ms, refocusing FA = 150°, matrix size = 320×320, FOV = 220 mm, slice thickness/gap = 2/0.4 mm, and 30 slices. The vendor-provided SMS sequence was used, which acquired separate coil calibration data for each slice (see supplementary material for visualization). Additionally, fully sampled T2-FSE data were acquired as a reference for desired image quality.
- 2) Prospectively SMS-accelerated gradient echo single-shot EPI data from six healthy subjects at MB4R2, MB2R2, and MB1R1 (i.e., no acceleration), using a 3T GE scanner equipped with an 21-channel head coil. The vendor-provided SMS sequence was used and common scan parameters were matrix size = 128×128, FOV = 220 mm, slice thickness/gap = 3/0.3 mm, and 48 slices. For MB1R1, TR/TE = 4480/30 ms, FA = 90°; for MB2R2, TR/TE = 2240/30 ms, FA = 84°; for MB4R2, TR/TE = 1120/30 ms, FA = 71°.

For all in-house datasets, subjects provided written informed consent, in accordance with the approval from the Institutional Review Board of Shenzhen Technology University (reference number: SZTULL012021005).

TABLE I

QUANTITATIVE EVALUATION OF SMS RECONSTRUCTION (RETROSPECTIVE ACCELERATION). THE BEST RESULTS ARE MARKED IN **BOLD** AND SECOND-BEST UNDERLINED.

Acceleration	Method	fastMRI				Longgang			
		R2		R3		R2		R3	
		PSNR	SSIM	PSNR	SSIM	PSNR	SSIM	PSNR	SSIM
MB3	RO-GRAPPA	28.84±3.96	0.84±0.08	22.27±2.33	0.71±0.08	34.34±3.48	0.91±0.04	25.96±3.70	0.76±0.08
	SPSG	29.26±3.69	0.85±0.07	21.96±2.22	0.71±0.08	34.53±3.41	0.91±0.04	25.69±3.58	0.76±0.08
	L1-wavelet	25.49±2.06	0.85±0.05	22.59±1.88	0.80±0.06	28.83±2.51	0.89±0.04	24.29±2.24	0.84±0.05
	ROCK	30.68±2.68	<u>0.89±0.04</u>	25.68±2.34	0.83±0.05	<u>34.91±3.22</u>	<u>0.92±0.03</u>	27.92±2.67	0.87±0.05
	VarNet	<u>34.18±1.55</u>	0.96±0.01	<u>31.86±1.40</u>	<u>0.94±0.01</u>	33.46±1.53	0.95±0.02	<u>31.49±1.60</u>	<u>0.93±0.02</u>
	ROGER	37.10±2.29	0.96±0.02	34.02±2.14	0.95±0.02	37.25±2.87	0.95±0.02	34.78±2.43	0.94±0.03
MB4	RO-GRAPPA	24.76±3.71	0.76±0.10	20.71±1.78	0.67±0.08	30.77±3.52	0.86±0.05	22.60±3.06	0.69±0.08
	SPSG	25.05±3.68	0.77±0.10	20.51±1.68	0.67±0.08	31.04±3.46	0.86±0.05	22.22±2.93	0.68±0.08
	L1-wavelet	23.42±1.92	0.81±0.06	21.46±1.65	0.77±0.06	25.60±2.16	0.86±0.05	22.80±2.02	0.80±0.06
	ROCK	27.23±2.58	<u>0.85±0.05</u>	23.92±1.93	<u>0.80±0.05</u>	30.97±2.67	0.89±0.04	25.46±2.22	0.83±0.05
	VarNet	<u>32.16±1.67</u>	0.95±0.02	<u>30.20±1.46</u>	0.93±0.01	<u>31.83±1.74</u>	<u>0.93±0.02</u>	<u>30.48±1.62</u>	<u>0.91±0.03</u>
	ROGER	35.18±2.51	0.95±0.02	31.32±2.16	0.93±0.02	36.13±2.63	0.95±0.02	32.21±2.16	0.92±0.03

B. Method Comparison and Implementation Details

We compared our method with k-space interpolation techniques (RO-GRAPPA [2] and SPSG [7]), traditional iterative methods (L1-wavelet SENSE [48] and ROCK [9]), and a supervised deep learning method, end-to-end variational network (VarNet) [16].

For RO-GRAPPA, SPSG, L1-wavelet, and ROCK, we used the central 64×64 k-space region as the calibration signal. For L1-wavelet and ROCK, we estimated coil sensitivity maps (CSMs) using the ESPIRiT [48] method from the central 30×30 k-space region.

For deep learning methods, VarNet and our method (ROGER), models were trained on the official fastMRI brain training set. We removed the last four noisy slices from each volume, resulting in approximately 52k slice images for training. The models were then used to infer on all other datasets without retraining, except for SMS EPI, where light fine-tuning was performed.

For VarNet, paired SMS data and fully sampled data were created under the ROC framework and used to train VarNet weights for 50 epochs with the official settings [47]. For ROGER, multi-coil images were coil-combined using ESPIRiT and then used to train the diffusion generative model. The complex-valued images were split into real and imaginary components, each serving as a separate channel. Guidance scaling factor λ was set to 2 and the LFE size to 8. We adopted the UNet network with multi-resolution attention as the DDPM architecture, using code from guided diffusion [38], [49]. Training was conducted with forward/reverse step of 1000, learning rate of 1×10^{-4} , batch size of 8, 2×10^5 iterations, and the Adam optimizer.

For the SMS EPI data, to address geometric distortion mismatch issue [27], [50], [51], MB1R1 data were used first to train GRAPPA kernels to reconstruct MB2R2 images, which were then to generate CSMs for MB4R2. This provides a better geometry match between the coil sensitivity maps and the SMS data due to the same in-plane acceleration factors.

C. Performance Evaluation

Peak signal-to-noise ratio (PSNR) and the structural similarity index (SSIM), were used to measure the reconstruction performance. Specifically, evaluations were performed between slices. The larger PSNR and SSIM, indicate a better reconstruction.

For prospective acceleration, no perfect ground truth is available due to potential subject motion, different geometry distortion and slightly different contrast. We visually evaluated the reconstructed image quality compared with fully sampled data and additionally calculated the tSNR maps for the EPI images using 50 frames.

V. RESULTS

This section presents both quantitative and qualitative reconstruction results. We first evaluate the methods on two retrospectively SMS-accelerated datasets. Next, we assess performance on unseen anatomical regions and prospectively SMS-accelerated FSE and EPI. Finally, the impact of EPI fine-tuning sample size and the effectiveness of the LFE module are analyzed.

A. Evaluation on Public and In-House Clinical Datasets

Table. I presents the quantitative reconstruction results for retrospective SMS acceleration on the fastMRI and Longgang datasets. Our method ROGER achieved the highest scores at all acceleration factors for both datasets.

Representative reconstruction results are presented in Fig. 2. GRAPPA and SPSG exhibited noticeable reconstruction noise, while L1-wavelet SENSE and ROCK showed aliasing artifacts. The results of VarNet were satisfactory, with a higher signal-to-noise ratio and fewer aliasing artifacts than traditional methods. However, VarNet failed to reconstruct many fine details and erroneously presents some white matter lesions as fake structures. In contrast, our method demonstrated the highest reconstruction quality, clearly revealing anatomical structures and small white matter lesions.

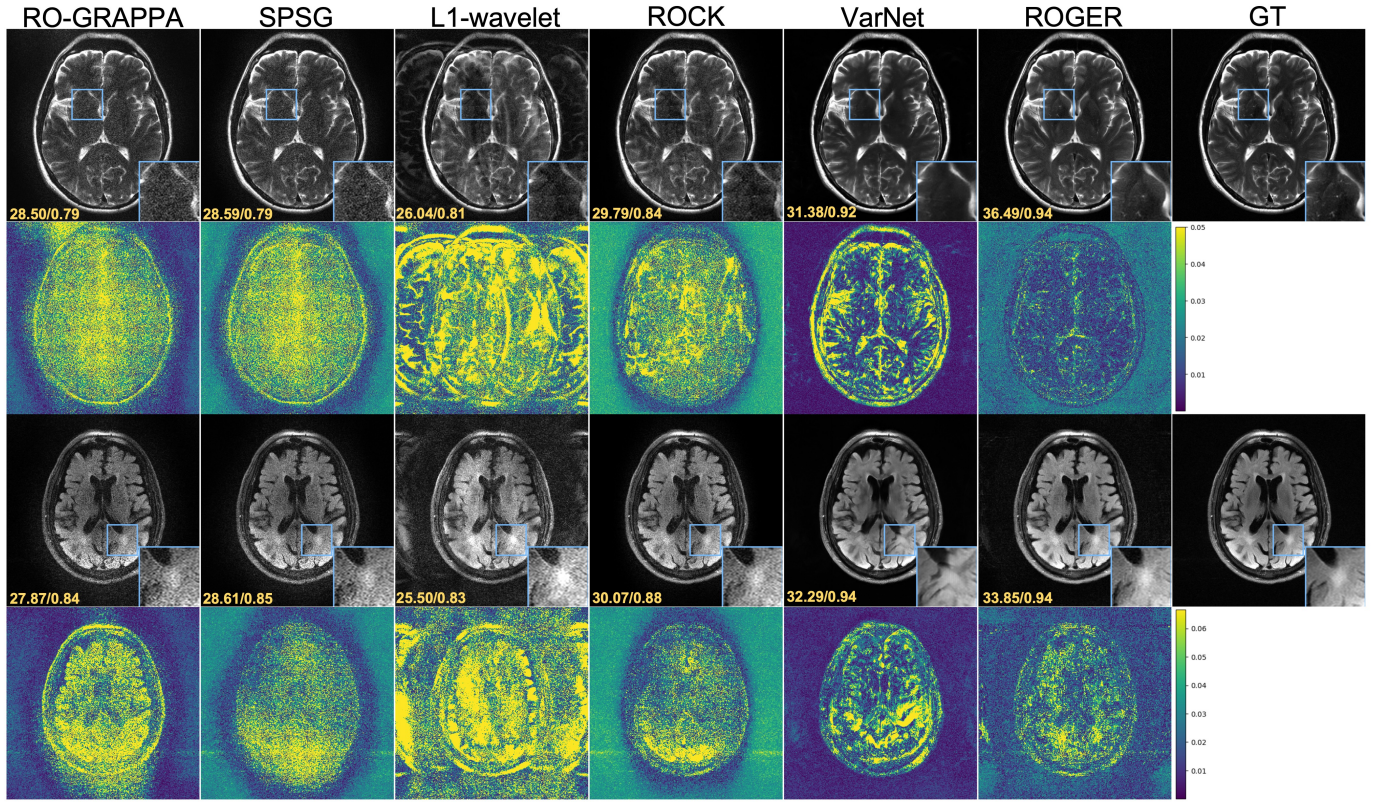


Fig. 2. Reconstructed images of retrospective SMS acceleration at MB4R2 in comparison with the ground truth (GT). The first and third rows are reconstructed images from the **fastMRI** and **Longgang** datasets, respectively, and their corresponding error maps are shown in the second/fourth rows. Yellow numbers represent PSNR/SSIM scores. Full visualizations across all slices/subjects are available in the supplementary materials.

B. Evaluation on Unseen Brain Regions

TABLE II

QUANTITATIVE EVALUATION OF SMS RECONSTRUCTION ON THE **HUAXIN** DATASETS WITH WHOLE BRAIN COVERAGE. THE BEST RESULTS ARE MARKED IN **BOLD** AND SECOND-BEST UNDERLINED.

Acceleration	MB3R2		MB4R2	
Metrics	PSNR	SSIM	PSNR	SSIM
RO-GRAPPA	34.30±3.19	0.92±0.04	31.37±2.73	0.89±0.05
SPSG	34.61±3.23	0.93±0.04	31.80±2.80	0.89±0.05
L1-wavelet	29.13±2.76	0.90±0.05	26.33±2.22	0.87±0.06
ROCK	<u>35.05±3.00</u>	0.94±0.03	<u>32.07±2.62</u>	0.91±0.04
VarNet	32.30±2.57	0.95±0.02	30.48±2.61	0.93±0.03
ROGER	36.49±3.48	0.96±0.02	35.37±3.12	0.95±0.02

Since the fastMRI training data does not contain slices more than 5mm below the orbital rim [47], we used the retrospectively accelerated Huaxin dataset, covering the whole brain, including the cerebellum and brainstem, to evaluate our method on unseen anatomical regions. As indicated by the mean PSNR/SSIM values in Table II and the visualization in Fig. 2 at MB4R2 acceleration, our algorithm achieved the best results among all methods again, despite not being trained on the inferior brain regions. Slice-level analysis presented in Fig. 3 revealed that our algorithm maintained superior performance on all slices with stable PSNR/SSIM advantages.

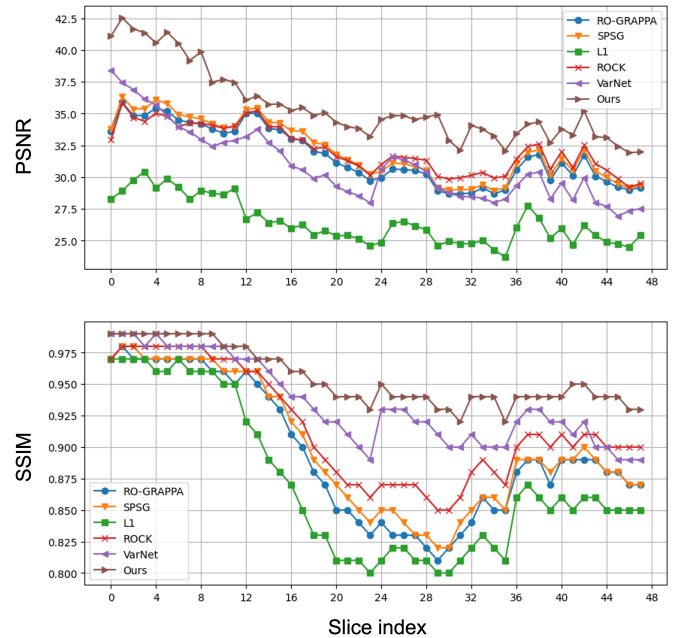


Fig. 3. Slice-wise PSNR and SSIM analysis for different methods at MB4R2 on one subject of the **Huaxin** dataset.

C. Evaluation on Prospectively Accelerated SMS FSE

The results of prospective SMS FSE acceleration agree with the findings with retrospective acceleration. As presented in

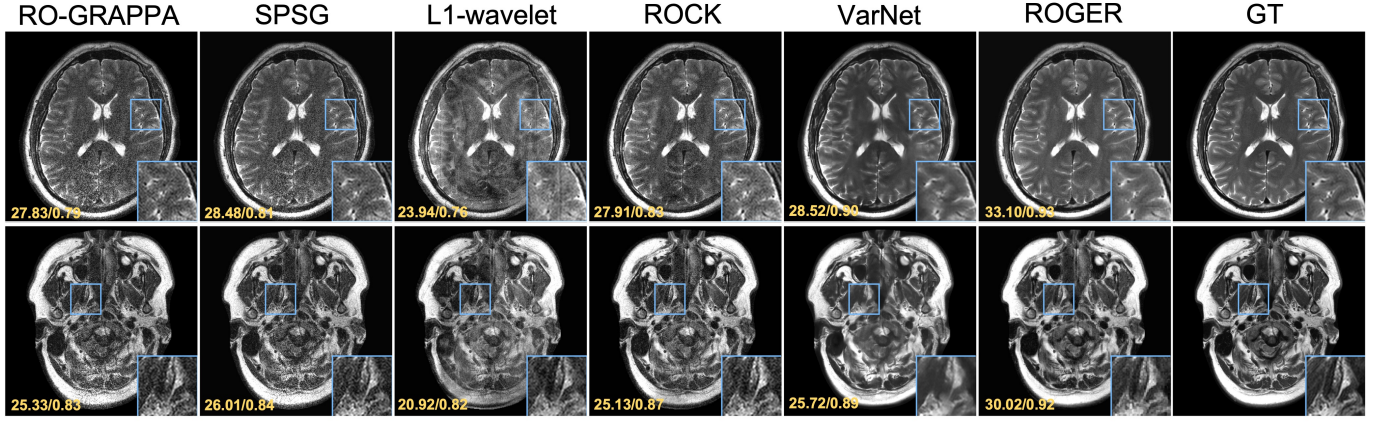


Fig. 4. Reconstructed images of retrospective SMS acceleration at MB4R2 on the **Huaxin** dataset with full brain coverage. Yellow numbers represent PSNR/SSIM scores. Two representative slices are presented with ground truth (GT). Our method ROGER remained robust on the brainstem area which was not present in the training set (fastMRI). Full visualizations across all slices/subjects are available in the supplementary materials.

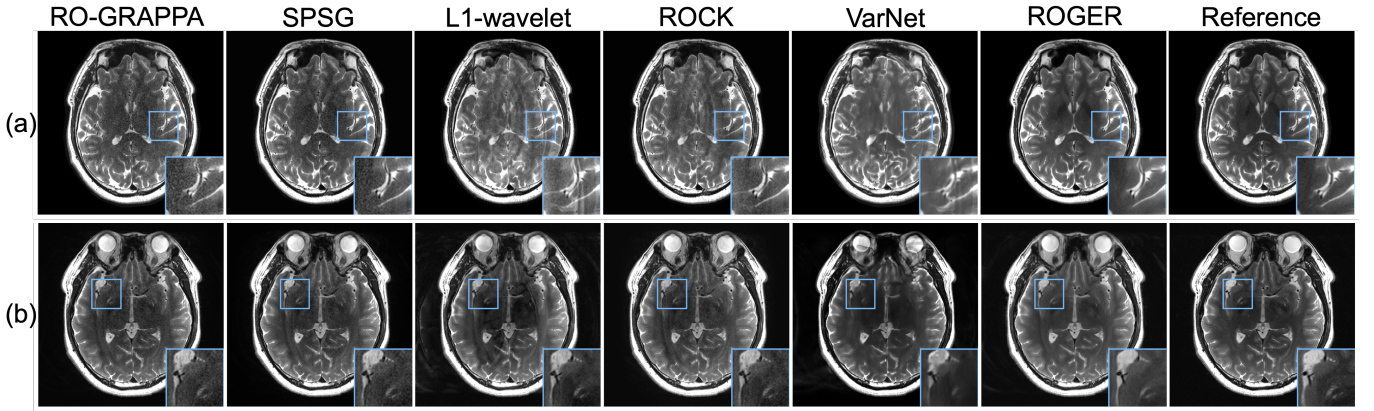


Fig. 5. (a) Reconstruction of prospectively SMS-accelerated FSE at MB3R3. (b) Reconstruction of prospectively SMS-accelerated FSE data at MB4R2. The reference images were acquired by a fully sampled scan. Full visualizations across all slices/subjects are available in the supplementary materials.

Fig. 5, at MB3R3 and MB4R2 acceleration, RO-GRAPPA and SPSG had similar results, both exhibiting heavy noise amplification. L1-wavelet SENSE and ROCK showed considerable aliasing artifacts.

Directly applying the fastMRI trained VarNet resulted in excessive aliasing artifacts in prospectively SMS-accelerated data (not shown in Fig. 5, available in the supplementary materials as "VarNet-Plain"). This issue likely arises because, during training, the calibration signal and SMS data had consistent image phases. However, in real-world SMS-accelerated data, the phases of the calibration signal and the SMS data are rarely perfectly aligned, leading to poor generalization of VarNet. As a workaround, we used the reconstruction results of RO-GRAPPA as calibration for VarNet, enabling it to perform reconstruction with reasonable results. Still, such improved VarNet suffered from residual artifacts and blurring on small structures as revealed by the enlarged views in Fig. 5.

In contrast, our method produced high-quality results that closely resembled the reference structure. This was achieved without any modifications to the fastMRI trained model or inference procedure.

D. Evaluation on Prospectively Accelerated SMS EPI

EPI is an ultra-fast imaging sequence, and has very different tissue contrast, image phase distribution, geometry distortion, and matrix sizes to regular anatomical images such as T2-FSE [27]. Therefore, for SMS EPI reconstruction using deep learning methods (i.e., VarNet and ROGER), we randomly selected 3 out of the 6 subjects as the training samples to fine-tune the model from fastMRI weights. From each subject, only one frame of the MB1R1 images and one frame of the GRAPPA reconstructed MB2R2 images were used for fine-tuning after discarding the top and bottom three slices. Thus, in total, only 252 slice images were used for fine-tuning. We used a learning rate of 1×10^{-4} , batch size of 8, iterations of 4×10^4 , and Adam optimizer.

The MB4R2 EPI data from the remaining three subjects were used as test set. As shown in Fig. 6, our method ROGER resulted in remarkably higher SNR and fewer artifacts than other methods. Moreover, our reconstruction led to consistently high tSNR across all brain regions.

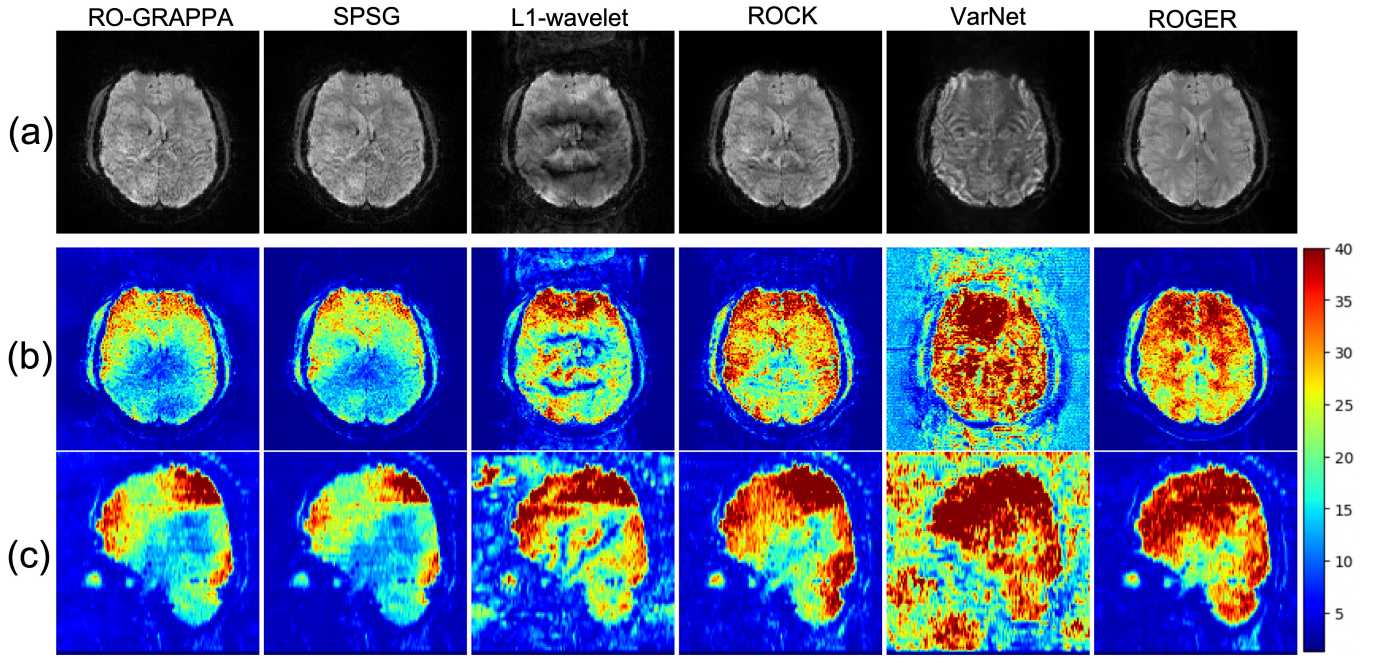


Fig. 6. (a) Reconstruction of prospectively SMS-accelerated EPI at MB4R2. (b) The corresponding tSNR maps computed from 50 frames. (c) The sagittal view of tSNR maps. Full visualizations across all slices/subjects are available in the supplementary materials.

E. Impact of Sample Sizes on EPI Fine-Tuning

In addition, we studied the impact of fine-tuning sample size on SMS EPI reconstruction quality. Fig. 7 shows the reconstruction results of one subject without fine-tuning ROGER and with fine-tuning using data from one, three, and five subjects, respectively. Without fine-tuning, the fastMRI-trained model produced noticeable artifacts due to large differences between EPI and anatomical imaging. Fine-tuning with one subject immediately improved image quality. Fine-tuning with three subjects resulted in further improvements, with no noticeable artifacts, while using five subjects yielded similar quality as three subjects. These results indicate that our method has strong generalization ability and can be applied to different datasets with minimal training resources.

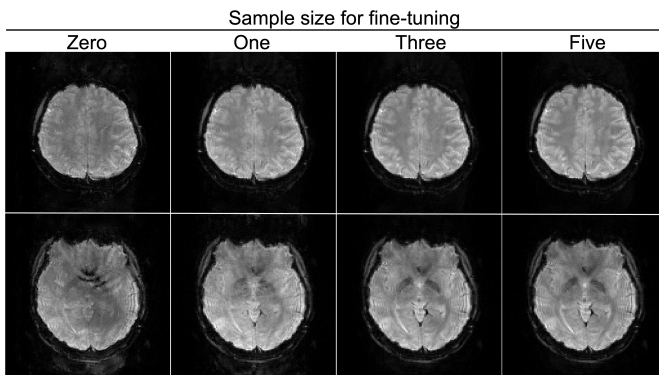


Fig. 7. The impact of fine-tuning sample sizes on the SMS EPI reconstruction at MB4R2. Decent reconstruction quality can be achieved with fine-tuning on three or more subjects.

F. Effect of LFE Module

Fig. 8 records the PSNR and SSIM scores of fastMRI reconstruction with different LFE sizes (i.e., sizes of GRAPPA interpolated k-space). As the LFE size increased from 0 (not using LFE) to approximately 8 (the setting in this study), our method showed marked improvement. However, excessively increasing the LFE size is not advisable, as the model performance declined with LFE sizes larger than 12, likely due to the interpolation errors introduced by the LFE module. Such decline was more pronounced for higher acceleration (MB3R3 and MB4R3) than lower acceleration (MB3R2 and MB4R2). Nevertheless, a stable range for the LFE size existed between 4 and 12, across various acceleration factors, to consistently achieve high SNR and SSIM scores. This observation is also visualized in Fig. 9.

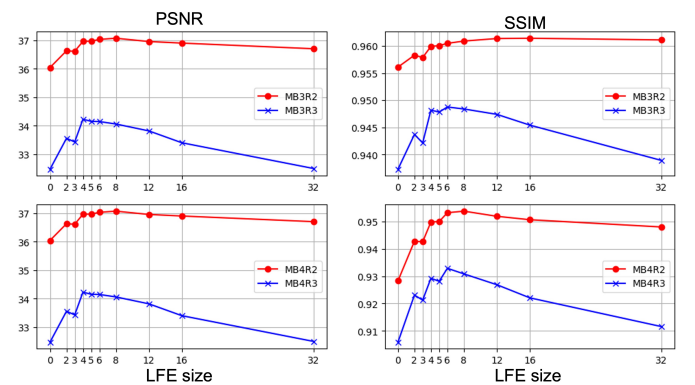


Fig. 8. The impact of LFE sizes on the mean PSNR/SSIM scores of the reconstructed images using the fastMRI dataset.

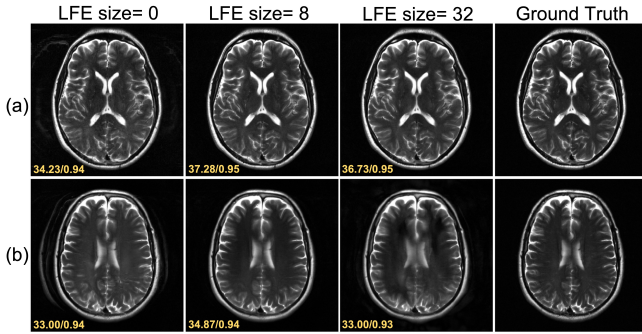


Fig. 9. Visualization of the impact of different LFE sizes on the reconstruction results on the **fastMRI** dataset (a) MB4R2 acceleration. (b) MB4R3 acceleration. Yellow numbers represent PSNR/SSIM scores.

VI. DISCUSSION

Our study introduces a novel approach SMS MRI reconstruction by integrating readout concatenation (ROC) with deep generative priors using denoising diffusion probabilistic models (DDPM). Our method outperforms existing techniques, achieving higher PSNR and SSIM while preserving anatomical details and reducing artifacts under various conditions.

Our method utilizes the ROC framework to apply data consistency terms, and reverses the ROC operation before applying the generative prior in each iteration. This approach ensures that data consistency terms are enforced properly while allowing the deep generative prior to be trained routinely on single-slice images without specific adjustments for SMS tasks. Without such decoupling, the prior would require complicated training on ROC images.

Another key innovation in our method is the low-frequency enhancement (LFE) module, which enhances reconstruction quality, especially at high acceleration factors. In principle, the LFE module can also be implemented with other methods [52]–[54], and its optimization constitutes future studies.

Deep learning has profoundly impacted MRI reconstruction, yet ensuring robustness across diverse scanning conditions remains a challenge. These variations include differences in scanner hardware, imaging sequences, and scanning parameters. Through validation on multiple datasets, our method is demonstrated highly robust against most of these factors without necessitating retraining. Even for challenging scenarios on EPI, minimal fine-tuning is sufficient. While our method provides a strong foundation, optimal performance in specialized applications might still benefit from tailored strategies [55]. The potential for broader applications, including cardiac [9], knee [29], and abdominal imaging [28], suggests exciting avenues for future research.

Our method has a few limitations. It relies on coil sensitivity maps (CSMs) estimated using ESPIRiT [48], whose performance varies with calibration data quality. Additionally, the current setting of 1000 iterations incurs high computational loads for reconstruction (2–3 min/slice on an RTX 4090 GPU). Improving CSM estimation and reconstruction speed [56], [57] are crucial for future research.

VII. CONCLUSION

In this study, we proposed a robust image reconstruction method for SMS MRI. It offers superior image reconstruction quality and high generalization ability, potentially benefiting a wide range of applications.

REFERENCES

- [1] F. A. Breuer, M. Blaimer, R. M. Heidemann, M. F. Mueller, M. A. Griswold, and P. M. Jakob, “Controlled aliasing in parallel imaging results in higher acceleration (caipirinha) for multi-slice imaging,” *Magn. Reson. Med.*, vol. 53, no. 3, pp. 684–691, 2005.
- [2] S. Moeller, A. T. Vu, E. Auerbach, K. Ugurbil, and E. Yacoub, “Ro extended fov sense/grappa for multiband imaging with fov shift,” in *Proc. Int. Soc. Magn. Reson. Med. (ISMRM)*, p. 4396, 2014.
- [3] K. Setsompop, B. A. Gagoski, J. R. Polimeni, T. Witzel, V. J. Wedeen, and L. L. Wald, “Blipped-controlled aliasing in parallel imaging for simultaneous multislice echo planar imaging with reduced g-factor penalty,” *Magn. Reson. Med.*, vol. 67, no. 5, pp. 1210–1224, 2012.
- [4] M. Barth, F. Breuer, P. J. Koopmans, D. G. Norris, and B. A. Poser, “Simultaneous multislice (sms) imaging techniques,” *Magn. Reson. Med.*, vol. 75, no. 1, pp. 63–81, 2016.
- [5] M. Blaimer, F. A. Breuer, N. Seiberlich, M. F. Mueller, R. M. Heidemann, V. Jellus, G. Wiggins, L. L. Wald, M. A. Griswold, and P. M. Jakob, “Accelerated volumetric mri with a sense/grappa combination,” *J. Magn. Reson. Imaging*, vol. 24, no. 2, pp. 444–450, 2006.
- [6] S. Moeller, E. Yacoub, C. A. Olman, E. Auerbach, J. Strupp, N. Harel, and K. Ugurbil, “Multiband multislice ge-epi at 7 tesla, with 16-fold acceleration using partial parallel imaging with application to high spatial and temporal whole-brain fmri,” *Magn. Reson. Med.*, vol. 63, no. 5, pp. 1144–1153, 2010.
- [7] S. F. Cauley, J. R. Polimeni, H. Bhat, L. L. Wald, and K. Setsompop, “Interslice leakage artifact reduction technique for simultaneous multislice acquisitions,” *Magn. Reson. Med.*, vol. 72, no. 1, pp. 93–102, 2014.
- [8] S. Rosenzweig, H. C. M. Holme, R. N. Wilke, D. Voit, J. Frahm, and M. Uecker, “Simultaneous multi-slice mri using cartesian and radial flash and regularized nonlinear inversion: Sms-nlinv,” *Magn. Reson. Med.*, vol. 79, no. 4, pp. 2057–2066, 2018.
- [9] O. B. Demirel, S. Weingärtner, S. Moeller, and M. Akçakaya, “Improved simultaneous multislice cardiac mri using readout concatenated k-space spirit (rock-spirit),” *Magn. Reson. Med.*, vol. 85, no. 6, pp. 3036–3048, 2021.
- [10] S. Park and J. Park, “Sms-hsl: simultaneous multislice aliasing separation exploiting hankel subspace learning,” *Magn. Reson. Med.*, vol. 78, no. 4, pp. 1392–1404, 2017.
- [11] E. J. Lim, T. Shin, J. Lee, and J. Park, “Generalized self-calibrating simultaneous multi-slice mr image reconstruction from 3d fourier encoding perspective,” *Med. Image Anal.*, vol. 82, p. 102621, 2022.
- [12] Ö. B. Demirel, S. Weingärtner, S. Moeller, and M. Akçakaya, “Improved simultaneous multi-slice imaging with composition of k-space interpolations (sms-cookie) for myocardial t1 mapping,” *PLoS one*, vol. 18, no. 7, p. e0283972, 2023.
- [13] D. Liang, J. Cheng, Z. Ke, and L. Ying, “Deep magnetic resonance image reconstruction: Inverse problems meet neural networks,” *IEEE Signal Processing Magazine*, vol. 37, no. 1, pp. 141–151, 2020.
- [14] H. K. Aggarwal, M. P. Mani, and M. Jacob, “Modl: Model-based deep learning architecture for inverse problems,” *IEEE Trans. Med. Imaging*, vol. 38, no. 2, pp. 394–405, 2018.
- [15] K. Hammernik, T. Klatzer, E. Kobler, M. P. Recht, D. K. Sodickson, T. Pock, and F. Knoll, “Learning a variational network for reconstruction of accelerated mri data,” *Magn. Reson. Med.*, vol. 79, no. 6, pp. 3055–3071, 2018.
- [16] A. Sriram, J. Zbontar, T. Murrell, A. Defazio, C. L. Zitnick, N. Yakubova, F. Knoll, and P. Johnson, “End-to-end variational networks for accelerated mri reconstruction,” in *Proc. Int. Conf. Med. Image Comput. Comput.-Assist. Intervent. (MICCAI)*, pp. 64–73, 2020.
- [17] J. Le, Y. Tian, J. Mendes, B. Wilson, M. Ibrahim, E. DiBella, and G. Adluru, “Deep learning for radial sms myocardial perfusion reconstruction using the 3d residual booster u-net,” *Magn. Reson. Imaging*, vol. 83, pp. 178–188, 2021.

- [18] O. B. Demirel, B. Yaman, L. Dowdle, S. Moeller, L. Vizioli, E. Yacoub, J. Strupp, C. A. Olman, K. Uğurbil, and M. Akçakaya, "20-fold accelerated 7t fmri using referenceless self-supervised deep learning reconstruction," in *Annu. Int. Conf. IEEE Eng. Med. Biol. Soc. (EMBC)*, pp. 3765–3769, 2021.
- [19] Y. Song, L. Shen, L. Xing, and S. Ermon, "Solving inverse problems in medical imaging with score-based generative models," in *Proc. Int. Conf. Learn. Represent. (ICLR)*, 2022.
- [20] A. Jalal, M. Arvinte, G. Daras, E. Price, A. G. Dimakis, and J. Tamir, "Robust compressed sensing mri with deep generative priors," *Adv. Neural Inf. Process. Syst.*, vol. 34, pp. 14938–14954, 2021.
- [21] H. Chung and J. C. Ye, "Score-based diffusion models for accelerated mri," *Med. Image Anal.*, vol. 80, p. 102479, 2022.
- [22] G. Luo, M. Blumenthal, M. Heide, and M. Uecker, "Bayesian mri reconstruction with joint uncertainty estimation using diffusion models," *Magn. Reson. Med.*, vol. 90, no. 1, pp. 295–311, 2023.
- [23] A. Güngör, S. U. Dar, Ş. Öztürk, Y. Korkmaz, H. A. Bedel, G. Elmas, M. Ozbey, and T. Çukur, "Adaptive diffusion priors for accelerated mri reconstruction," *Med. Image Anal.*, p. 102872, 2023.
- [24] Y. Korkmaz, T. Cukur, and V. M. Patel, "Self-supervised mri reconstruction with unrolled diffusion models," in *Proc. Int. Conf. Med. Image Comput. Comput.-Assist. Intervent. (MICCAI)*, pp. 491–501, 2023.
- [25] C. Cao, Z.-X. Cui, Y. Wang, S. Liu, T. Chen, H. Zheng, D. Liang, and Y. Zhu, "High-frequency space diffusion model for accelerated mri," *IEEE Trans. Med. Imaging*, vol. 43, no. 5, pp. 1853–1865, 2024.
- [26] G. Luo, S. Huang, and M. Uecker, "Autoregressive image diffusion: Generating image sequence and application in mri," *arXiv preprint arXiv:2405.14327*, 2024.
- [27] O. Viessmann and J. R. Polimeni, "High-resolution fmri at 7tesla: challenges, promises and recent developments for individual-focused fmri studies," *Current Opinion in Behavioral Sciences*, vol. 40, pp. 96–104, 2021. Deep Imaging - Personalized Neuroscience.
- [28] Z. Ye, S. Yao, T. Yang, Q. Li, Z. Li, and B. Song, "Abdominal diffusion-weighted mri with simultaneous multi-slice acquisition: Agreement and reproducibility of apparent diffusion coefficients measurements," *J. Magn. Reson. Imaging*, vol. 59, no. 4, pp. 1170–1178, 2024.
- [29] J. Fritz, B. Fritz, J. Zhang, G. K. Thawait, D. H. Joshi, L. Pan, and D. Wang, "Simultaneous multislice accelerated turbo spin echo magnetic resonance imaging: comparison and combination with in-plane parallel imaging acceleration for high-resolution magnetic resonance imaging of the knee," *Invest. Radiol.*, vol. 52, no. 9, pp. 529–537, 2017.
- [30] J. Zhang, Z. Yi, Y. Zhao, L. Xiao, J. Hu, C. Man, V. Lau, S. Su, F. Chen, A. T. Leong, *et al.*, "Calibrationless reconstruction of uniformly-undersampled multi-channel mr data with deep learning estimated esprit maps," *Magn. Reson. Med.*, vol. 90, no. 1, pp. 280–294, 2023.
- [31] S. Moeller and S. Banerjee, "Chapter 7 - simultaneous multislice reconstruction," in *Magnetic Resonance Image Reconstruction* (M. Akçakaya, M. Doneva, and C. Prieto, eds.), vol. 7 of *Advances in Magnetic Resonance Technology and Applications*, pp. 159–187, Academic Press, 2022.
- [32] D. J. Larkman, J. V. Hajnal, A. H. Herlihy, G. A. Coutts, I. R. Young, and G. Ehnholm, "Use of multicoil arrays for separation of signal from multiple slices simultaneously excited," *J. Magn. Reson. Imaging*, vol. 13, no. 2, pp. 313–317, 2001.
- [33] K. Zhu, R. F. Dougherty, H. Wu, M. J. Muddione, A. M. Takahashi, T. Zhang, J. M. Pauly, and A. B. Kerr, "Hybrid-space sense reconstruction for simultaneous multi-slice mri," *IEEE Trans. Med. Imaging*, vol. 35, no. 8, pp. 1824–1836, 2016.
- [34] M. A. Griswold, P. M. Jakob, R. M. Heidemann, M. Nittka, V. Jellus, J. Wang, B. Kiefer, and A. Haase, "Generalized autocalibrating partially parallel acquisitions (grappa)," *Magn. Reson. Med.*, vol. 47, no. 6, pp. 1202–1210, 2002.
- [35] P. J. Koopmans, "Two-dimensional-ngc-sense-grappa for fast, ghosting-robust reconstruction of in-plane and slice-accelerated blipped-caipi echo planar imaging," *Magn. Reson. Med.*, vol. 77, no. 3, pp. 998–1009, 2017.
- [36] M. Lyu, M. Barth, V. B. Xie, Y. Liu, X. Ma, Y. Feng, and E. X. Wu, "Robust sense reconstruction of simultaneous multislice epi with low-rank enhanced coil sensitivity calibration and slice-dependent 2d nyquist ghost correction," *Magn. Reson. Med.*, vol. 80, no. 4, pp. 1376–1390, 2018.
- [37] Y. Liu, M. Lyu, M. Barth, Z. Yi, A. T. Leong, F. Chen, Y. Feng, and E. X. Wu, "Pec-grappa reconstruction of simultaneous multislice epi with slice-dependent 2d nyquist ghost correction," *Magn. Reson. Med.*, vol. 81, no. 3, pp. 1924–1934, 2019.
- [38] P. Dhariwal and A. Nichol, "Diffusion models beat gans on image synthesis," *Adv. Neural Inf. Process. Syst.*, vol. 34, pp. 8780–8794, 2021.
- [39] J. Ho, A. Jain, and P. Abbeel, "Denoising diffusion probabilistic models," *Adv. Neural Inf. Process. Syst.*, vol. 33, pp. 6840–6851, 2020.
- [40] J. Song, C. Meng, and S. Ermon, "Denoising diffusion implicit models," in *Proc. Int. Conf. Learn. Represent. (ICLR)*, 2021.
- [41] G. Luo, X. Wang, M. Blumenthal, M. Schilling, E. H. U. Rauf, R. Kotikalapudi, N. Focke, and M. Uecker, "Generative image priors for mri reconstruction trained from magnitude-only images," *arXiv preprint arXiv:2308.02340*, 2023.
- [42] S. Huang, G. Luo, X. Wang, Z. Chen, Y. Wang, H. Yang, P.-A. Heng, L. Zhang, and M. Lyu, "Noise level adaptive diffusion model for robust reconstruction of accelerated mri," *arXiv preprint arXiv:2403.05245*, 2024.
- [43] T. Garber and T. Tirer, "Image restoration by denoising diffusion models with iteratively preconditioned guidance," in *Proc. IEEE/CVF Conf. Comput. Vis. Pattern Recognit.*, pp. 25245–25254, 2024.
- [44] Y. Wang, J. Yu, and J. Zhang, "Zero-shot image restoration using denoising diffusion null-space model," in *Proc. Int. Conf. Learn. Represent. (ICLR)*, 2023.
- [45] B. Kawar, M. Elad, S. Ermon, and J. Song, "Denoising diffusion restoration models," *Adv. Neural Inf. Process. Syst.*, vol. 35, pp. 23593–23606, 2022.
- [46] J. Song, A. Vahdat, M. Mardani, and J. Kautz, "Pseudoinverse-guided diffusion models for inverse problems," in *Proc. Int. Conf. Learn. Represent. (ICLR)*, 2023.
- [47] J. Zbontar, F. Knoll, A. Sriram, T. Murrell, Z. Huang, M. J. Muckley, A. Defazio, R. Stern, P. Johnson, M. Bruno, *et al.*, "fastmri: An open dataset and benchmarks for accelerated mri," *arXiv preprint arXiv:1811.08839*, 2018.
- [48] M. Uecker, P. Lai, M. J. Murphy, P. Virtue, M. Elad, J. M. Pauly, S. S. Vasanawala, and M. Lustig, "Esprit—an eigenvalue approach to autocalibrating parallel mri: where sense meets grappa," *Magn. Reson. Med.*, vol. 71, no. 3, pp. 990–1001, 2014.
- [49] A. Q. Nichol and P. Dhariwal, "Improved denoising diffusion probabilistic models," in *Int. Conf. Machine Learning*, pp. 8162–8171, 2021.
- [50] J. R. Polimeni, H. Bhat, T. Witzel, T. Benner, T. Feiweier, S. J. Inati, V. Renvall, K. Heberlein, and L. L. Wald, "Reducing sensitivity losses due to respiration and motion in accelerated echo planar imaging by reordering the autocalibration data acquisition," *Magn. Reson. Med.*, vol. 75, no. 2, pp. 665–679, 2016.
- [51] M. Lyu, Y. Liu, and E. X. Wu, "Improved parallel imaging reconstruction of epi using inversely distortion corrected flash as calibration data," in *Proc. Int. Soc. Magn. Reson. Med. (ISMRM)*, p. 3509, 2018.
- [52] M. Lustig and J. M. Pauly, "Spirit: Iterative self-consistent parallel imaging reconstruction from arbitrary k-space," *Magn. Reson. Med.*, vol. 64, no. 2, pp. 457–471, 2010.
- [53] M. Akçakaya, S. Moeller, S. Weingärtner, and K. Uğurbil, "Scan-specific robust artificial-neural-networks for k-space interpolation (raki) reconstruction: Database-free deep learning for fast imaging," *Magn. Reson. Med.*, vol. 81, no. 1, pp. 439–453, 2019.
- [54] C. Zhang, S. Moeller, O. B. Demirel, K. Uğurbil, and M. Akçakaya, "Residual raki: A hybrid linear and non-linear approach for scan-specific k-space deep learning," *NeuroImage*, vol. 256, p. 119248, 2022.
- [55] S. Huang, J. Li, Y. Wang, Z. Chen, S. Liu, Y. Liu, Y. Xiong, B. Wu, J. Liu, H. Guo, E. X. Wu, and M. Lyu, "Zero-shot epi nyquist ghost correction with diffusion-based generative models and magnitude consistency regularization," in *Proc. Int. Soc. Magn. Reson. Med. (ISMRM)*, p. 0353, 2024.
- [56] H. Chung, S. Lee, and J. C. Ye, "Decomposed diffusion sampler for accelerating large-scale inverse problems," in *Proc. Int. Conf. Learn. Represent. (ICLR)*, 2024.
- [57] Q. Gao, Z. Li, J. Zhang, Y. Zhang, and H. Shan, "Corediff: Contextual error-modulated generalized diffusion model for low-dose ct denoising and generalization," *IEEE Trans. Med. Imaging*, vol. 43, no. 2, pp. 745–759, 2024.